A new oxynitride-based solid state Z-scheme photocatalytic system for efficient Cr(VI) reduction and water oxidation

Yansong Zhou, Gang Chen [*], Yaoguang Yu, Lichen Zhao, Jingxue Sun, Fang He, Hongjun Dong

Department of Chemistry, Harbin Institute of Technology, Harbin 150001, China

A B S T R A C T

Achieving ideal photocatalytic systems by mimicking Z-scheme mechanism in natural photosynthesis results in highly efficient artificial photosynthesis. A new oxynitride-based solid state Z-scheme photocatalytic system containing $(Ga_xZn1_{-x})(N_xO1_{-x})$ and $Nb_{3.49}N_{4.56}O_{0.44}$ was constructed. $Nb_{3.49}N_{4.56}O_{0.44}/(Ga_xZn1_{-x})(N_xO1_{-x})(6.0)$ exhibits the highest rate for complete reduction of Cr(VI) within 30 min under simulated sunlight irradiation as well as extremely high apparent quantum efficiency of 68% at 350 nm 24.4% at 420 nm for photocatalytic water oxidation. A similar solid state Z-scheme photocatalytic system was also obtained when compositing $Nb_{3.49}N_{4.56}O_{0.44}$ with TaON. It's expected that $Nb_{3.49}N_{4.56}O_{0.44}$ can also be composed with other oxynitride semiconductor to construct more oxynitride-based solid state Z-scheme photocatalytic systems.

© 2015 Elsevier B.V. All rights reserved.

1. Introduction

Direct conversion of the clean and abundant solar energy to chemical energy through artificial photosynthesis is a highly desirable approach to power the sustainable planet [1]. However, the major challenges that limit the energy conversion efficiency in artificial photosynthesis process are: (a) utilization of the longer-wavelength light; (b) separation efficiency of the photogenerated charge carriers in the photocatalysts; (c) the appropriate redox potential of the photogenerated charge carriers matching that of the reactants. Inspired by the Z-scheme mechanism in natural photosynthesis, constructing a Z-scheme type photocatalyst driven by Z-scheme mechanism using two different semiconductor photocatalysts may overcome the aforementioned problems [2]. During the past decades, great achievements have been obtained in artificial photosynthesis over various Z-scheme type systems for water-splitting [3–7] and organic dye degradation [8–11]. Unfortunately, most of these systems contain redox pairs leading to some obvious drawbacks such as the backward reactions between the redox pairs and the effective photogenerated charge carriers which restrict the further improvement of the photocatalytic efficiency. Thus constructing redox pair-free Z-scheme photocatalytic systems

could be an effective way to overcome these drawbacks in the redox pairs containing system [12].

Since the concept of all-solid-state Z-scheme photocatalytic system was introduced in CdS–Au–TiO$_2$ photocatalysts in 2006, [13] intensive attention have been paid to constructing the heterojunction-type photocatalytic systems for the aim of achieving Z-scheme photocatalytic systems due to their aforementioned advantages [14]. Unfortunately, only a limited number of the as-fabricated heterojunction-type photocatalysts in some certain systems were turned out to be Z-scheme photocatalystic systems [15–17]. So far, one of the crucial challenge that limits the constructing of efficient solid state Z-scheme photocatalystic systems is to choose appropriate semiconductors as electron collector and hole collectors in the heterojunction-type photocatalytic system, which is intrinsically determined by the difference of the band structure between the composited semiconductors [18]. Therefore, the development of semiconductor candidates with appropriate band positions for a wide range of semiconductor photocatalysts to fabricate solid state Z-scheme photocatalytic system with high solar energy conversion efficiency is of great importance.

(Oxy)nitrides are regarded as suitable candidate photocatalysts owing to their narrow bandgaps, suitable band edge positions, and high stability under light irradiation [19]. $Nb_{3.49}N_{4.56}O_{0.44}$ is a narrow electron band semiconductor with partially non-localized d electrons [20]. Otherwise, $Nb_{3.49}N_{4.56}O_{0.44}$ was determined to be an n-type semiconductor with a relatively negative Fermi level which is more negative than those of most other (oxy) nitrides. Therefore,

* Corresponding author. Fax: +86 451 86413753.
E-mail address: gchen@hit.edu.cn (G. Chen).

after being composited with another oxynitride semiconductors, the $Nb_{3.49}N_{4.56}O_{0.44}$ side tend to be positive charged with its band bending up at the interface, which means that the photogenerated electrons in the conduction band of another semiconductor tend to be transfer to $Nb_{3.49}N_{4.56}O_{0.44}$ side and recombine with the holes in the valence band of $Nb_{3.49}N_{4.56}O_{0.44}$ under light illumination [21]. Eventually, the photogenerated charge carriers were efficiently separated in the composited systems as well as the maintaining of their original high redox capability. Otherwise, similar elements, namely N and O, make it easy to form a well contact interface between $Nb_{3.49}N_{4.56}O_{0.44}$ and other (oxy) nitrides, which is essential for the transfer of the charge carriers between them. Inspired by this, it is expected that Z-scheme systems in solid state could be constructed by compisiting $Nb_{3.49}N_{4.56}O_{0.44}$ with another (oxy) nitride semiconductor photocatalysts as well as photoelectronic application. To the best of our knowledge, there is no report about $Nb_{3.49}N_{4.56}O_{0.44}$ for solar energy conversion application.

In this work, all oxynitride-based solid state Z-scheme photocatalytic systems were constructed for the first time. $Nb_{3.49}N_{4.56}O_{0.44}$ was composited with $(Ga_xZn1_{-x})(N_xO1_{-x})$ (GZNO)— an effective visible light active photocatalysts for water splitting with outstanding stability in the presence of cocatalysts [22–24]. The two semiconductors showed a well-composited feature that is good for charge carrier separation and transfer between them. We demonstrated that the NbNO/GZNO composite functions as an Cr(VI) reduction as well as O_2 evolution photocatalyst respectively without loading of any cocatalysts under simulated sunlight irradiation. The NbNO/GZNO(6.0) sample shows the highest performance for completely photocatalytic reduction of the Cr(VI) within 30 min among the compisiting serises. Meanwhile, the NbNO/GZNO(6.0) sample also yielded high AQE of 68% at 350 nm 24.4% for photocatalytic water oxidation under a monochromatic light of 420 nm respectively. Otherwise, another oxynitride-based Z-scheme photocatalystic system $Nb_{3.49}N_{4.56}O_{0.44}$/TaON with lower charger carrier recombination efficiency and enhanced photocatalytic water oxidation performance has also been constructed. These findings demonstrate the constructing of nature-inspired solid-state artificial photocatalytic system using $Nb_{3.49}N_{4.56}O_{0.44}$ and another (oxy) nitrides for the effective solar energy harvesting and conversion.

2. Experimental section

2.1. Preparation of photocatalysts

All of the samples were prepared through a high temperature solid state method. Briefly, a mixture of 0.29 mmol of Ga_2O_3 (99.99%, Aladding Chemistry Co. Ltd), 0.58 mmol of ZnO (99.99%, Aladding Chemistry Co. Ltd) powders and a certain amount of Nb_2O_5 (99.99%, Aladding Chemistry Co. Ltd) were nitrided at 1123 K for 15 h under NH_3 flow ($\sim$100 mL min^{-1}) after being ground for 30 min in an agate mortar. The amount of Nb_2O_5 was determined by setting the percentage of Nb atoms to the total amount of Ga atoms in Ga_2O_3 and Zn atoms in ZnO as different amount namely 0 (GZNO), 2.0 (GZNO/NbNO(2.0)), 4.0 (GZNO/NbNO(4.0)), 6.0 (GZNO/NbNO(6.0)), 8.0 (GZNO/NbNO(8.0)), 10.0 (GZNO/NbNO(10.0)). The samples were collected after being cooled to room temperature under NH_3 flow. The compositing material can also be prepared by nitriding the mixture powder of $(Ga_xZn_{1-x})(N_xO_{1-x})$ and Nb_2O_5 under the similar condition. $Nb_{3.49}N_{4.56}O_{0.44}$ and TaON were prepared through the same method.

The sample of $Nb_{3.49}N_{4.56}O_{0.44}$/TaON (5.0) was prepared using TaON and Nb_2O_5 as raw materials. Typically, mixture containing 2.0 mmol TaON and 0.1 Nb_2O_5 mmol were heated under the ammo-

nia atmosphere ($\sim$100 mL min^{-1}) for 15 h. Finally, the powder was collected after being cooled to roomtemperature under NH_3 flow.

2.2. Characterization

The crystal structure of the samples was characterized with a powder X-ray diffractometer (XRD, Rigaku D/max-2000) using Cu-Kα radiation (λ = 0.15406 nm, 45 kV, 50 mA). Transmission electron microscope equipped with EDX system (TEM, FEI Tecnai G^2) working at 300 kV was employed to observe the morphology and characterize the chemical composition of the samples. The high angle annular dark fields (HAADF) detector forms a Z-contrast image and scanning transmission electron microscopy (STEM) image operated in the mode. UV–vis absorption spectra were recorded on a spectrophotometer (TU-1901) using Ba_2SO_4 as reference. The surface photovoltaic spectra were collected on an assembled instrument (Jilin University) equipped with a lock-in amplier (SR830, Stanford). XPS measurements were carried out on a K-Alpha XPS spectrometer (PHI 5700 ESCA System), using Al Kα X-ray radiation (1486.6 eV) for excitation. Carbon C1s line with position at 284.6 eV was used as a reference to correct the charging effect. The photoluminescence (PL) measurements were carried out at room temperature with a luminescence spectrometer (Perkin-Elmer, LS-55) using 325 nm as excitation wavelength. Time-resolved PL spectra were recorded on FluoroMax$^{\circledR}$-4 Fluorescence Spectrophotometer from HORIBA scientific under 301 nm excitation at room temperature. A double first-order exponential decay "biexponential" model was used to fit both decay curves as follows: [25]

$$y = A_1 \exp\left(\frac{-t}{t_1}\right) + A_2 \exp\left(\frac{-t}{t_2}\right) + y_0$$

2.3. Photocatalytic reactions

2.3.1. Photocatalytic water oxidation

The photocatalytic reactions were performed in a vacuum-closed gas-circulation system with a top window. The photocatalyst powder (50 mg) was ultrasonically dispersed for 10 min in ultrapure water (18 MΩ) $AgNO_3$ (0.1 mol L^{-1}) for O_2 evolution respectively. The reaction was carried out at 278 K by irradiating the suspension with light from a 300 W Xe lamp (PLS-SXE300/300UV) equipped with an AM 1.5G filter (100 mW/cm^{-2}). Prior to irradiation, the reaction mixture was evacuated for 30 min in order to remove dissolved gases. The amount of produced gases ere measured by gas chromatography (Agilent 7890) with a thermal conductivity detector (TCD), taking Ar as carrier gas.

Apparent quantum yields (AQY) for water oxidation with a two-photon excitation process were measured under the same experimental condition, except for the equipment of band pass filters with different wavelength. The apparent quantum yields are defined by following eqs [3,26]:

$$AQY(\%) = \frac{\text{Number of reacted electrons}}{\text{Number of incident photons}} \times 100$$

$$= \frac{2 \times 4 \times \text{number of } O_2 \text{molecules evolved}}{\text{Number of incident photons}} \times 100$$

The number of incident photons was measured by a radiometer with different models for UV and visible-light regions (Photoelectric Instrument Factory, Beijing Normal University).

2.3.2. Photocatalytic Cr(VI) reduction

Aqueous chromium species has two stable oxidation states, Cr(VI) and Cr(III) [27,28]. In the medium to low pH range, Cr(V1) exists in aqueous solution predominantly as the dichro-
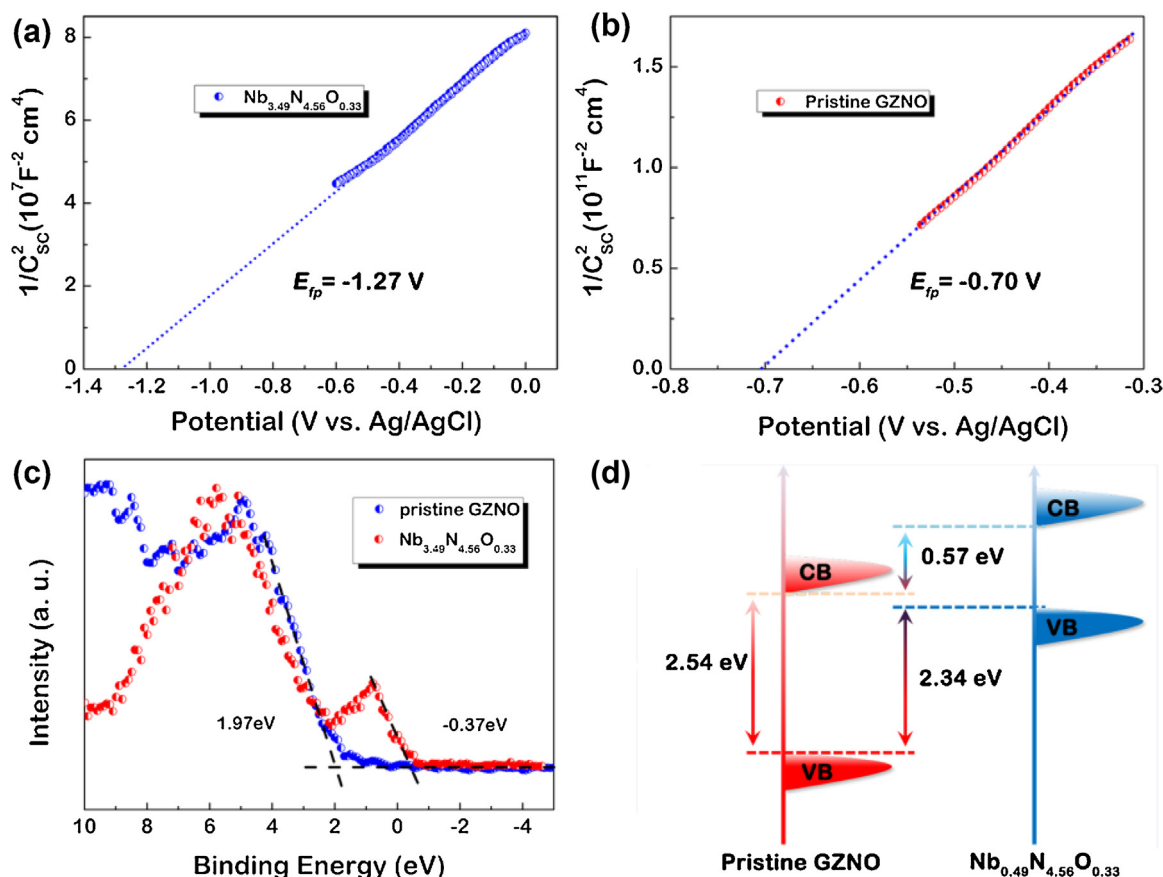
Fig. 1. Mott–Schottky plots of $Nb_{3.49}N_{4.56}O_{0.44}$ (a) and pristine GZNO (b). (c) Valence-band XPS spectra of GZNO and $Nb_{3.49}N_{4.56}O_{0.44}$. (d) Schematic illustration of the band alignment of GZNO and $Nb_{3.49}N_{4.56}O_{0.44}$.

mate anion $Cr_2O_7^{2-}$, which is reduced to Cr(II1) by the following reaction $Cr_2O_7^{2-} + 14H^+ + 6e^- \rightarrow 2Cr^{3+} + 7H_2O$[29]. The photocatalytic Cr(VI) reduction experiments was carried out according to Yang et al. [30]. In a typical process, 50 mg of the as-prepared photocatalyst was dispersed into 100 mL of $K_2Cr_2O_7$ solution with the concentration of Cr(VI) of 10 mg L^{-1} and 0.05 mL lactic acid ultrasonically for 10 min. The pH value of the suspension was about 2.5. The suspension was further stirred for 1 h in the dark to reach adsorption equilibrium before photocatalytic reaction. 3 mL of the sample were taken from the suspension at given time intervals and centrifuged at 10,000 rpm for 10 min, The Cr(VI) reduction was determined colorimetrically at 540 nm using the diphenylcarbazide (DPC) method. In detail, 1 mL of the supernatant was mixed with 9 mL of 0.2 M H_2SO_4 in a 50 mL volumetric beaker. Subsequently, 0.2 mL of freshly prepared 0.25% (w/v) DPC in acetone was added to the beaker. The mixture was kept still for 10–15 min for complete color development after been vigorously shaken for 30 s. The solution analyzed by UV–vis absorption spectroscopy (TU-1900). Blank experiments were conducted through the same procedure but without addition of photocatalyst.

2.4. Platinum photodeposition experiment

15 mg GZNO/NbNO(6.0) was ultrasonically dispersed for 10 min in an aqueous solution (100 mL) containing methanol (10 vol%) and 0.1 mL H_2PtCl_6 (1.5 mg mL^{-1}). Then then suspension was irradiated with light from a 300 W Xe lamp (PLS-SXE300/300UV) for 0.5 h. The powder was collected after been washed with water and enthanol three times.

2.5. Photoelectrochemistry characterization

The photoelectrochemical measurements were carried out using a standard three-electrode cell with a Ag/AgCl (3.0 M KCl) reference electrode, a platinum foil as a counter electrode on a Autolab PGSTAT302N (ECO-Chemie) electrochemical workstation. Na_2SO_4 (0.5 M, pH 4.5, adjusted by H_2SO_4) was used as the electrolyte solution. The working electrode was prepared by spin coating method on a 20 mm × 30 mm fluorine doped tin oxide (FTO). The Mott–chottky plots of the samples were determined applying potentials in the range of −1.0 to 0 V versus a Ag/AgCl reference. Photocurrent curves were collected using 0.0 V bias under visible light (λ > 400 nm) irradiation using Na_2SO_4 (0.5 M, pH 4.5) containing methanol (10 vol%) as the electrolyte solution. AC impedance measurement was carried out using a 5.0 mV ac voltage signal in the 100 KHz to 1 Hz frequency range.

3. Results and discussion

Both $Nb_{3.49}N_{4.56}O_{0.44}$ and GZNO show characteristic of n-type semiconductors, whereas the flat band potential of the former is about 0.57 V more negative than that of the latter one (Fig. 1a,b), which suggests the higher Fermi energy level of $Nb_{3.49}N_{4.56}O_{0.44}$. The density of states (DOS) of the valence band for $Nb_{3.49}N_{4.56}O_{0.44}$ and GZNO were also investigated by valence band XPS (Fig. 1c). $Nb_{3.49}N_{4.56}O_{0.44}$ displays an edge of valence band maximum (VBM) at −0.37 eV, which is 2.34 eV lower than that of GZNO. Combined with the results of optical band gap of GZNO (∼2.54 eV, Fig. S1), it can be suggested that the VBM of $Nb_{3.49}N_{4.56}O_{0.44}$ is approximately 0.2 eV lower than the conduction band minimum (CBM) of GZNO.
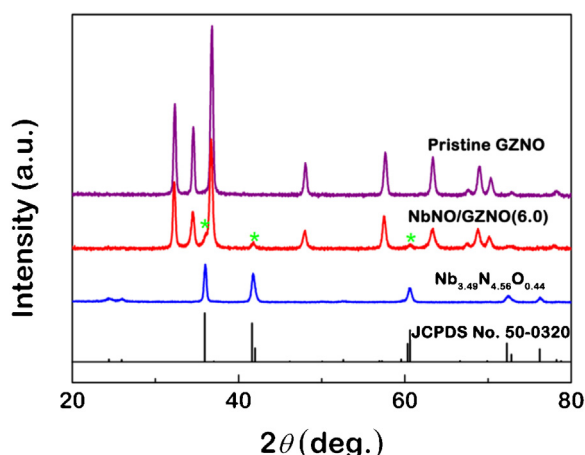
Fig. 2. XRD patterns of GZNO (purple), NbNO/GZNO(6.0) (red) and $Nb_{3.49}N_{4.56}O_{0.44}$ (blue). The presence of all the peaks attributed to $Nb_{3.49}N_{4.56}O_{0.44}$ and GZNO confirm the existence of the two compositing phases. (For interpretation of the references to colour in this figure legend, the reader is referred to the web version of this article.)

Fig. 3. TEM images ((a), (b) and (e)) and HRTEM images (c), (d) of NbNO/GZNO(6.0). EDX point analysis for points i and ii in panel b (f).

Therefore, once the junction between $Nb_{3.49}N_{4.56}O_{0.44}$ and GZNO formed, electrons will flow from NbNO to GZNO, resulting in a built-in electric field with its direction pointing to the GZNO side under thermal equilibrium at the interface [14,18,31]. As a result, the photogenerated charge carriers will be efficiently seperated driven by the interface electric field, which may be beneficial to the enhancement of the photocatalytic efficiency. The schematic illustration of the band alignment of GZNO and $Nb_{3.49}N_{4.56}O_{0.44}$ is shown in Fig. 1d.

The crystal structures of the as-prepared GZNO and $Nb_{3.49}N_{4.56}O_{0.44}$ samples were investigated by XRD (Fig. 2). Pristine GZNO was identified as single-phase wurtzite-type structure that is similar to hexagonal ZnO and GaN but with peak shifting [32]. For sample prepared from nitriding Nb_2O_5, all XRD peaks could be well indexed as the crystalline tetragonal form of $Nb_{3.49}N_{4.56}O_{0.44}$ (JCPDS No. 50-0320). The XRD pattern of NbNO/GZNO(6.0) contained all of the peaks observed in the $Nb_{3.49}N_{4.56}O_{0.44}$ and GZNO patterns. Peaks attributed to impurities other than $Nb_{3.49}N_{4.56}O_{0.44}$ and GZNO are not observed, indicating that no new phase formatted after the compositing process. The relatively low intensity for NbNO is mainly due to its low content in sample of of NbNO/GZNO(6.0).

The chemical composition change in GZNO have also been investigated by EDX between pristine GZNO and GZNO component in NbNO/GZNO(6.0). As listed in Table 1, similar N/O ratios were determined to be 2.30 for pristine GZNO and 2.24 for GZNO component in NbNO/GZNO(6.0). No obvious changes in chemiccal composition of GZNO in pristine GZNO and NbNO/GZNO(6.0), indicating that $Nb_{3.49}N_{4.56}O_{0.44}$ compositing showed little effects on the chemcal compositon of GZNO during the silimar preparation process. The crystal lattice parameters are sensitive to the chemical composition in GZNO. However, no shift in the main peaks of GZNO between pristine GZNO and NbNO/GZNO(6.0) was observed further confirmed that little change happened in the chemical composition for GZNO after the compositing process.

Fig. 3a presents the TEM image of NbNO/GZNO(6.0) in which some small particles whose diameters are less than 50 nm attaching on saface of the larger hollow ones are observed. The detailed structure was further clearly shown at a much higher magnification (Fig. 3b). Besides, results from the corresponding selected area electron diffraction (SADE) analysis reveal the exitence of $Nb_{3.49}N_{4.56}O_{0.44}$ and GZNO (Fig. S2) in this structure. Furthermore, the composition of the big and small particles was analysised by energy dispersive X-ray spectroscopy (EDX) point analysis respec-
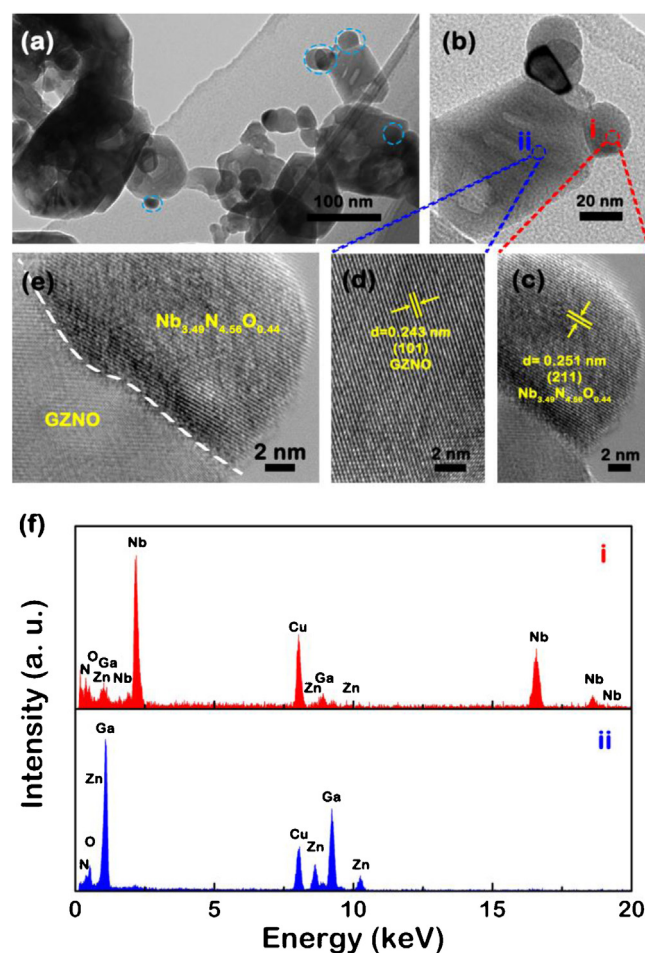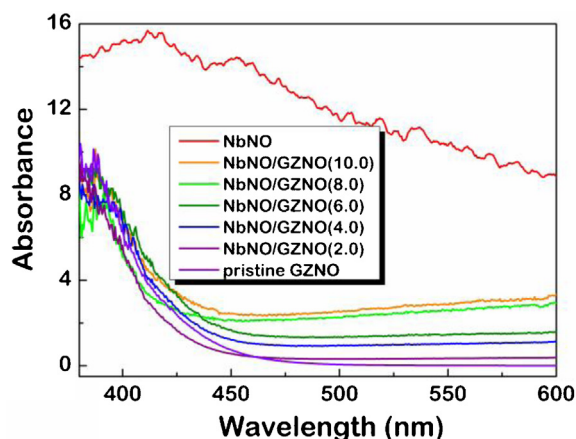
tively at two points (i and ii) as marked in Fig. 3b,f. Strong signals from Nb and relatively low signal from Zn and Ga are observerved in the spectrum of point i, whereas opposite case happens in the spectrum for point ii. Combined with the results from XRD, it can be concluded that the big hollow particles are GZNO, while the smaller ones attached on the surface of the big ones are $Nb_{3.49}N_{4.56}O_{0.44}$. These results are further confirmed by the high-resolution TEM analysis as crystal lattice fringes with the distances of 0.234 nm and 0.251 nm matched well with the (1 0 1) plane of GZNO (Fig. 3d) and (2 1 0) plane of $Nb_{3.49}N_{4.56}O_{0.44}$ (Fig. 3c) respectively. Otherwise, a tightly contact interface with clear crystal lattice but without amorphous phase between $Nb_{3.49}N_{4.56}O_{0.44}$ and GZNO particles is clearly observed in Fig. 3e, which may provide effective contact for the interparticle charge carrier transfer. While, compositing of $Nb_{3.49}N_{4.56}O_{0.44}$ showed little effects on the optical absorption edge of GZNO but enhance the visible light absorption when increase the compositing amount of $Nb_{3.49}N_{4.56}O_{0.44}$ (Fig. 4). While, compositing of $Nb_{3.49}N_{4.56}O_{0.44}$ showed little effects on the optical absorption edge of GZNO but enhance the visible light absorption when increase the compositing amount of $Nb_{3.49}N_{4.56}O_{0.44}$ due to the strong adsorption capability of visible light of $Nb_{3.49}N_{4.56}O_{0.44}$ (Fig. 4), which is a common phenomena in gaphene composited photocatalysts [33,34]. Therefore, a heterostructure consisting GZNO and $Nb_{3.49}N_{4.56}O_{0.44}$ was sucessfully prepared in this work.

Photoluminescence (PL) measurements were carried out to investigate charge separation and transfer behaviours in NbNO/GZNO heterostructure. Time-resolved PL experiments characterizing the charge carrier dynamics (Fig. 5a) shows the longest
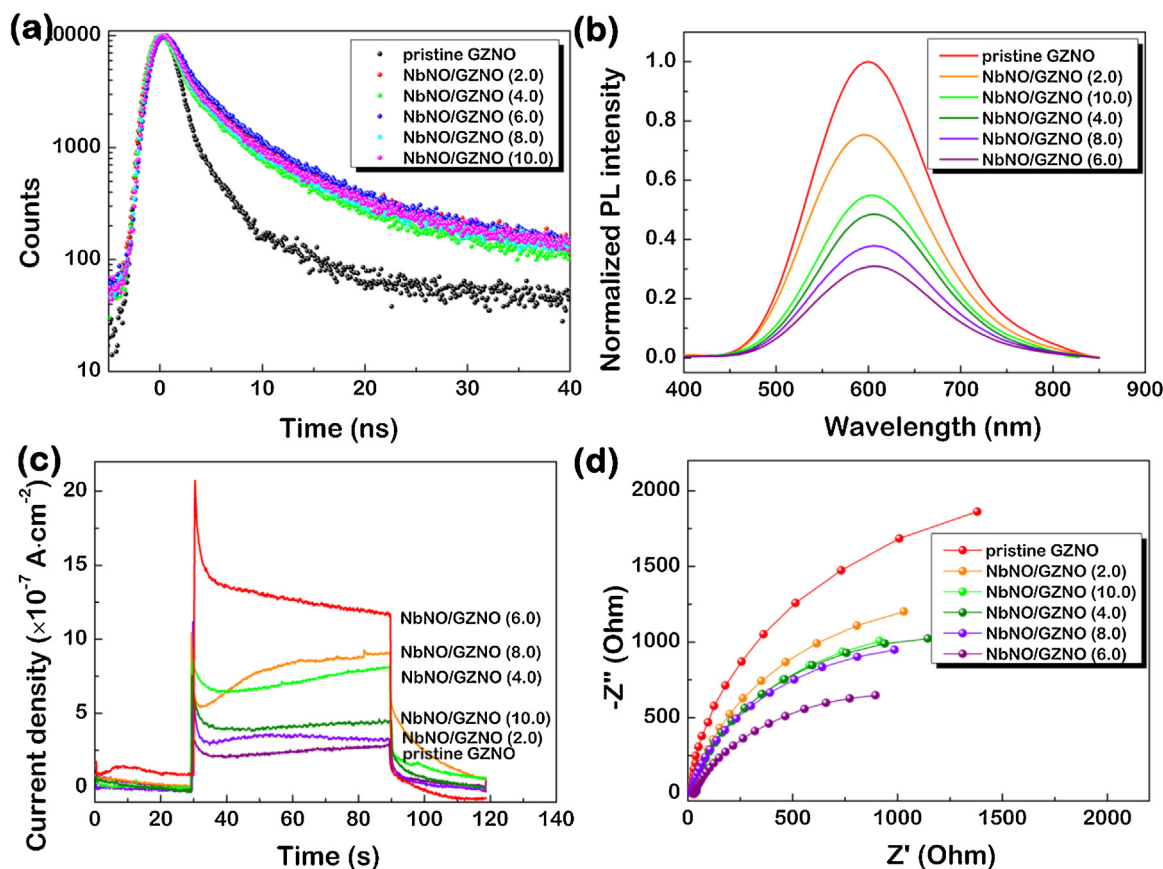
Table 1
Chemical compositions of GZNO in pristine GZNO and GZNO component in NbNO/GZNO(6.0) determined by EDX.

Samples	Atomic%				N/O ratio
	Ga	Zn	N	O	
Pristine GZNO	34.38	9.95	38.82	16.83	2.30
GZNO (NbNO/GZNO(6.0))	34.64	10.08	38.21	17.04	2.24

Fig. 4. UV–Vis spectra of NbNO/GZNO with different $Nb_{3.49}N_{4.56}O_{0.44}$ compositing contents.

lifetime, which is beneficial for the photocatalytic reactions since the longer lifetime means more chance for the charge carriers to react with the water molecules or other reactants rather than the fast recombination of electrons and holes. The time-resolved PL decay curves of all samples can be well fitted into biexponential function with shorter decay lifetime attributed to the the nonradiative relaxation process relevant to defects and the longer decay lifetime coming from the radiative process which is relevant to the recombination of photogenerated holes and electrons [35,36]. In NbNO/GZNO(6.0), the photogenerated electron in GZNO transfer to the interface and recombine with the photogenerated holes in $Nb_{3.49}N_{4.56}O_{0.44}$ with a further nonradiative process. Due to the build-in interfacial electronic field, seperation of the photogenerated charge carriers is accerlated with prolonged lifetimes in NbNO/GZNO(6.0). In addition, Broad PL spectra of GZNO and other samples at the range of 450 nm–850 nm are obserbed, which originate from the Zn-related acceptor levels in GZNO (Fig. 5b) [37,38]. The PL signals decrease remarkably compared to that of GZNO when composited with $Nb_{3.49}N_{4.56}O_{0.44}$, indicating the lower recombination efficiency of the charge carrier. The effects of charge carrier separation behavior were also investigated by photoelectrochemical measurements. The highest improvement in transient photocurrent responses of NbNO/GZNO(6.0) is obserbed compared to that of pristine GZNO (Fig. 5c), which corresponds to the highest photogenerated charge carrier separation efficiency in NbNO/GZNO(6.0). Meanwhile, the kinetics of interfacial charge immigration was further investigated by electrochemical

Fig. 5. Charge carrier separation behaviour of GZNO composited with different amount of $Nb_{3.49}N_{4.56}O_{0.44}$. (a) Time–resolved PL and (b) PL spectra under 301 nm excitation at room temperature. (c) transient photocurrent responses and (d) EIS Nyquist plots of pristine GZNO and NbNO/GZNO(6.0) under simulated sunlight irradiation.
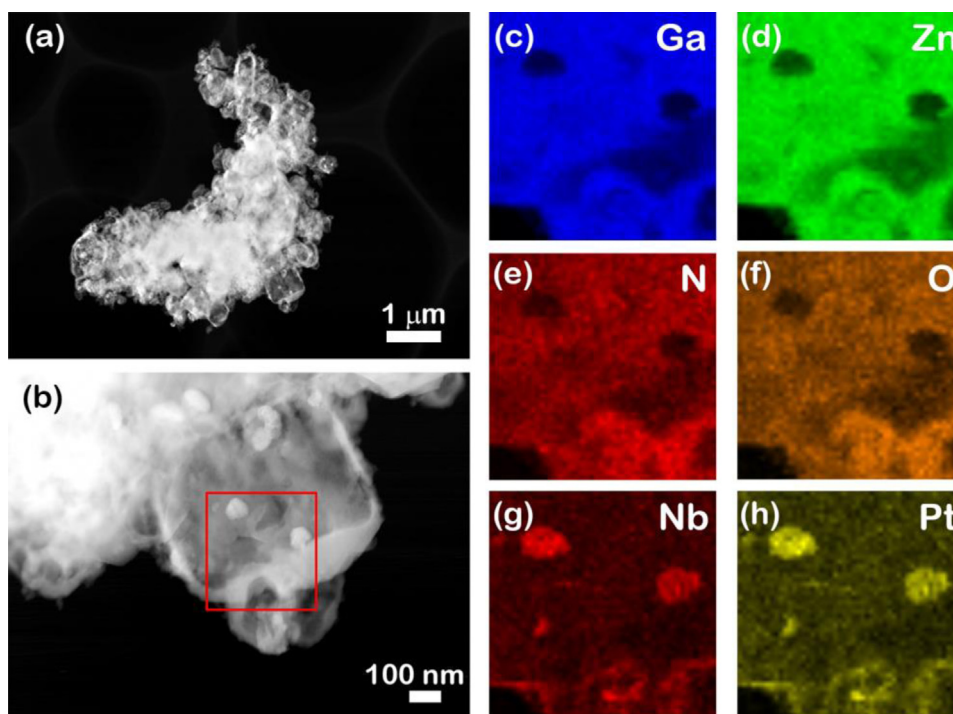
Fig. 6. (a) HAADF Z-contrast image, (b) high resolution HAADF Z-contrast image and EDX mapping images corresponding to the area marked in (b) of NbNO/GZNO(6.0).

impedance spectroscopy (EIS) analysis [39]. As shown in Fig. 5d, compared to pristine GZNO, a significantly decreased diameter in the EIS Nyquist plots is observed in NbNO/GZNO samples, indicating more efficient separation and immigration of photogenerated electron−hole pairs in the compositing sample, which is in good accordance with the results of PL tests and photocurrent measurements.

In order to prove the Z-scheme process in NbNO/GZNO composites, a platinum photodeposition experiment was carried out. As shown in HAADF Z-contrast image, large amount of bright dots that distributed on the surface of the big particle can be clearly observed in Fig. 6. Combined with the results from TEM in Fig. 2, the smaller dots may be assigned to the $Nb_{3.49}N_{4.56}O_{0.44}$ phase since the amount of loaded Pt is relative low (1 wt%) in the sample. When observed in a magnified view, the contrast between the small and big particles can be clear distinguished (Fig. 6b), orginating from the difference in the Z value, which furth confirm the different composition between them. This elemental difference between the big and small particles were directly revealed by the EDX mapping as shown in Fig. 6c–h. Clearly, Nb concentrates on the small particle (Fig. 6g), in accordance with the TEM test (Fig. 3). Sigficantly, the loaded Pt shows similar distribution to Nb, which indicating that the photo generated electrons concerted on the $Nb_{3.49}N_{4.56}O_{0.44}$ phase. Therefore, results from platinum photodeposition experiment confirm directly that transport of the photo generated charge carriers in NbNO/GZNO composites is driven by Z scheme.

The surface photovoltage was carried out to further investigate the surface charge features of NbNO/GZNO(6.0) [40,41]. The positive signal for suggest the n-type characteristics of GZNO, in agreement with the results from Mott–Schottky polts. The remarkably reduced photovoltage signal suggests that the electrons tend to be more easy to concentrate on the surface of NbNO/GZNO(6.0), which means that the photogenerated electrons from CB of GZNO recombine with the holes of VB for $Nb_{3.49}N_{4.56}O_{0.44}$ (Fig. S3) driven by the Z-scheme, in accordance with the aforementioned analysis. Similar results have also been obtained in the CdS/WO_3 Z-scheme photocatalyst system [42]. The prolonged lifetime and reduced
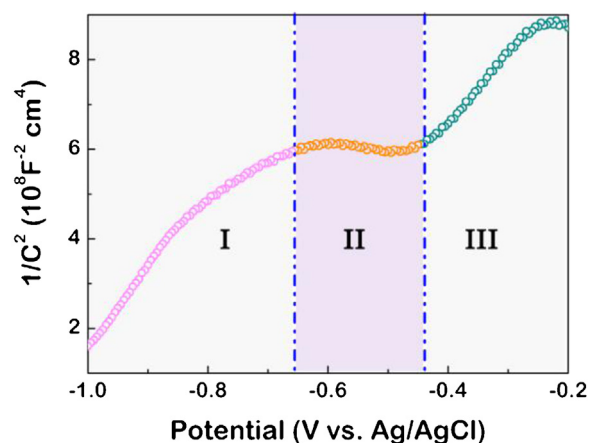

Fig. 7. Mott–Schottky plots of NbNO/GZNO(6.0) in 0.5 M Na_2SO_4 (pH 4.5) in a standard three electrode photoelectrochemical cell.

recombination efficiency imply the easy charge transfer of the charge carriers between $Nb_{3.49}N_{4.56}O_{0.44}$ and GZNO as a possible reason of the existence of quasi-continuous intermediate levels at the interface.

The presence of intermediate levels was experimentally confirmed by a Mott–Schottky plot of NbNO/GZNO(6.0). As shown in Fig. 7, the Mott–Schottky plot can be divided into three sections according to the different variations of capacitance versus potential. In section i and iii, it exhibits linear dependence with a positive slope as a typical feature of an n-type semiconductor. Interestingly, the capacitance is independent of voltage in section ii, as a clear feature of high density monoenergetic interface states located at the NbNO/GZNO(6.0) junction [43–45]. It's widely accepted that the high density monoenergetic interface states tend to be quasi-continuous with low electric resistance as the function that is similar to a conductor for the photogenerated charge carriers transfer driven by the interface potential from GZNO to
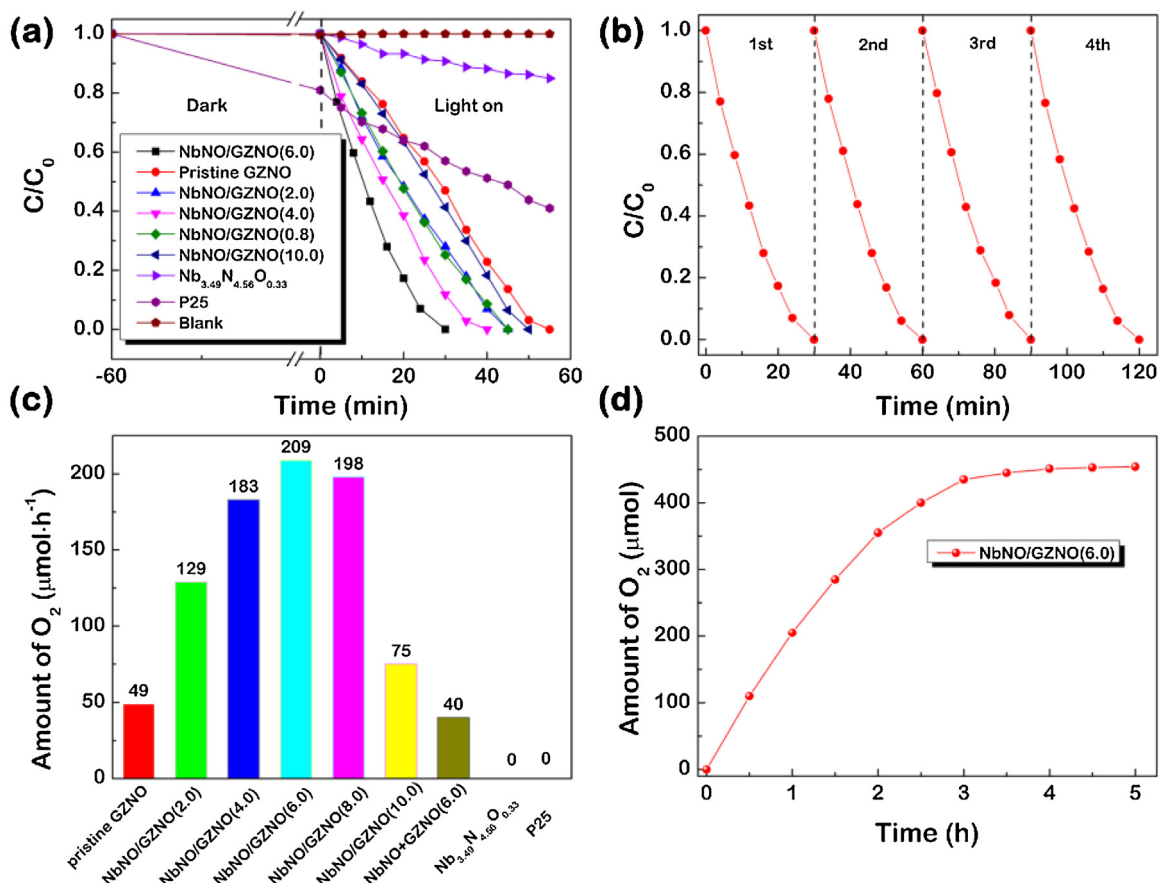
Fig. 8. Photocatalytic performance of the photocatalysts. (a) photocatalytic Cr(VI) reduction capability of all samples and (b) the recyclability of NbNO/GZNO(6.0), (c) photocatalytic water oxidation capability of all samples and (d) the time course Time course of photocatalytic O_2 evolution of bNO/GZNO(6.0) in the presence of $AgNO_3$ under simulated sunlight irradiation.

$Nb_{3.49}N_{4.56}O_{0.44}$, corresponding to the prelonged lifetime and the lower recombination efficeincy of the charge carrier. Therefore, a solid state Z-scheme photocatalytic system was prepared by compositing $Nb_{3.49}N_{4.56}O_{0.44}$ with GZNO without any electron media. The application of the as-prepared samples was investigeted by evluating their performance of photocatalytic reduction of Cr(VI) and oxidation of water under simulated sunlight irradiation.

Photocatalytic Cr(VI) reduction experiments were performed to investigate the reduction capability of all the samples (Fig. 8a). NbNO showed a weak performance for photocatalytic Cr(VI) reduction. When composited with GZNO, the performance was remarkably enhanced. Furthermore, GZNO was also demonstrated to be an effective photocatalyst for complete Cr(VI) reduction within 55 min under simulated sunlight irradiation. The performance was further improved when compositing GZNO with NbNO. The highest rate was obtained over NbNO/GZNO(6.0) for completely photocatalytic reduction of Cr(VI) within 30 min. The enhanced Cr(VI) reduction are mainly attributed to the high reduction capability as well as the effective charge separation between GZNO and $Nb_{3.49}N_{4.56}O_{0.44}$. Significatntly, the NbNO/GZNO(6.0) sample showed a highly efficient and stable capality for completely photocatalytic reduction of Cr(VI) even after four runs (Fig. 8b).

The oxidizability of the photogenerated holes in the as-prepared Z-scheme photocatalytic systems was evaluated by photocatalytic water oxidation (Fig. 8c). Pristine GZNO showed a relatively low O_2 generation rate possibly due to the high recombination rate of the photogenerated charge carriers. NbNO alone exhibits no activity of O_2 evolution because that the VBM of $Nb_{3.49}N_{4.56}O_{0.44}$ is far below the water water oxidation level. Interestingly, small
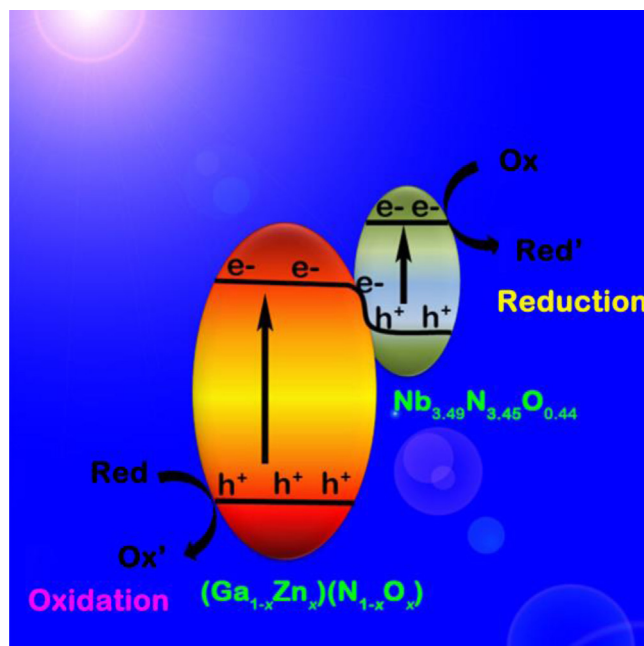

Fig. 9. Schematic of photocatalytic mechanism and charge transfer process in the Z-scheme NbNO/GZNO system.

amount of $Nb_{3.49}N_{4.56}O_{0.44}$ composited with GZNO can evidently enhance O_2 generation rate of GZNO. All these further confirm
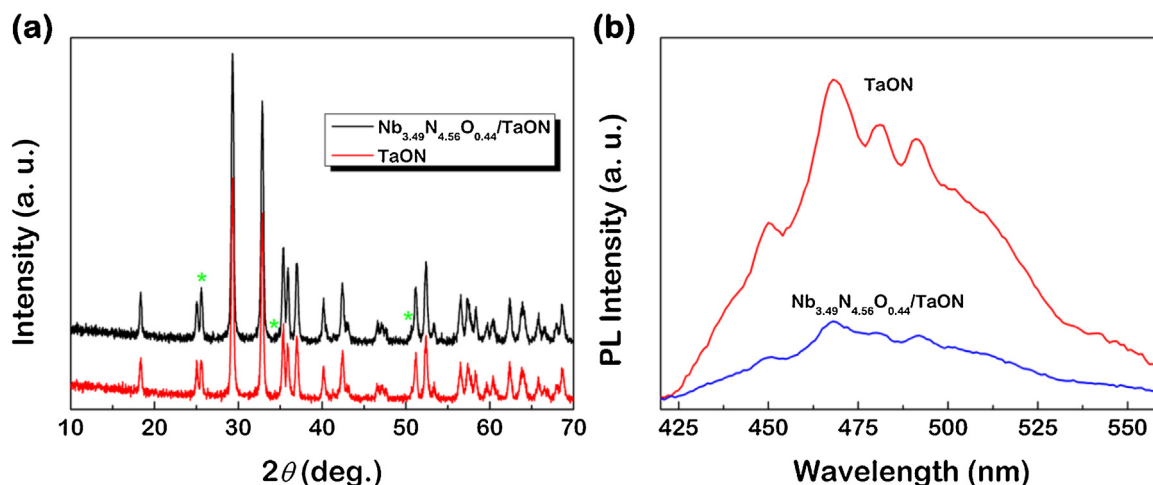
Fig. 10. (a)XRD patterns of TaON and $Nb_{3.49}N_{4.56}O_{0.44}$/TaON and (b) PL spectra of pristine TaON and $Nb_{3.49}N_{4.56}O_{0.44}$/TaON (5.0) obtained at room temperature.

the conclusion that the transfer mechanism of photogenerated charge carriers between $Nb_{3.49}N_{4.56}O_{0.44}$ and GZNO was driven by Z-scheme that photogenerated electrons in the CB of GZNO recombine with the holes in the VB of $Nb_{3.49}N_{4.56}O_{0.44}$. The sample NbNO/GZNO(6.0) showed the highest O_2 generation rate of 209 mol h^{-1}, which is about 4 times of that for pristine GZNO (49 mol h^{-1}). The AQE for NbNO/GZNO(6.0) was determined to be 68.0% (350 nm) and 24.4% (420 nm). However, redundant $Nb_{3.49}N_{4.56}O_{0.44}$ leads to decrease of O_2 evolution rate as the reasons that the shielding effect of $Nb_{3.49}N_{4.56}O_{0.44}$ due to its narrower bandgap compared to that of GZNO as well as the none active feature of $Nb_{3.49}N_{4.56}O_{0.44}$. As shown in Fig. 8d, the oxygen production activity for NbNO/GZNO(6.0) decreased quickly after 2 h of photocatalytic reaction. Such a trend is reasonable because the sacrificial reagent AgNO₃ was consumed by photogenerated electrons, resulting in the formation of silver metal. The generated silver metal was deposited on the surface of the photocatralyst, leading to retardation of light adsorption [46–48].

Based on the above results, the photocatalytic mechanism and charge transfer process in NbNO/GZNO photocatalytic systems are illustrated in Fig. 9. Upon photoexcitation, photogenerated electons in the conduction band of $(Ga_xZn1_{-x})(N_xO1_{-x})$ transfer to $Nb_{3.49}N_{4.56}O_{0.44}$ and recombine with the holes in the valence band of $Nb_{3.49}N_{4.56}O_{0.44}$ due to the interfacial electrinic filed and quasi-continuous intermediate levels at the interface. As a result, the lifetime of photogenerated holes in $(Ga_xZn1_{-x})(N_xO1_{-x})$ and electrons in $Nb_{3.49}N_{4.56}O_{0.44}$, which retain their original high redox capability to driven water oxidation and Cr(VI) reduction, become longer due to the lower probability of their recombination.

$Nb_{3.49}N_{4.56}O_{0.44}$ was also composited with TaON—a semiconductor that be widely used as photocatalyst and photoelectrode material [49–53] - to further confirm its feasibility as electron collector for other oxynitride semiconductors (Fig. 10a). Compared to that of pristine TaON, the remarkable enhanced photocatalytic water oxidation performance of $Nb_{3.49}N_{4.56}O_{0.44}$/TaON implies that the transfer of photogenerated charge carriers in this system were driven by the Z-scheme mechanism (28.1 mol h^{-1} for TaON and 44.2 mol h^{-1} for $Nb_{3.49}N_{4.56}O_{0.44}$/TaON (5.0)) as discussed before. Furthermore, recombination rate of the photogenerated charge carriers in $Nb_{3.49}N_{4.56}O_{0.44}$/TaON is significantly reduced as revealed by PL characterization (Fig. 10b), indicating the well separation of the electrons and holes between $Nb_{3.49}N_{4.56}O_{0.44}$ and TaON. This result further demonstrates the potential application of $Nb_{3.49}N_{4.56}O_{0.44}$ as an electron collector to construct a wide variety of (oxy) nitride-based solid state Z-scheme systems for solar energy

conversion applications. Further work is undergoing for the ultilization of $Nb_{3.49}N_{4.56}O_{0.44}$ as electron collector for other oxynitrides or even nitrides to construct more oxynitride-based Z-shceme photocatalystic systems for artificial photosynthesis application.

4. Conclusions

In conclusion, a new oxynitride-based solid state Z-scheme photocatalytic system including $Nb_{3.49}N_{4.56}O_{0.44}/(Ga_xZn1_{-x})(N_xO1_{-x})$ was reported in this work. This photocatalytic system enables photogenerated charge carriers to own sufficiently high redox potential with low charge recombination probability. Consequently, the system shows a highly efficient performance in photocatalytic Cr(VI) reduction under simulated sunlight irradiation and water oxidation in ultra violet as well as visible light region. Another solid state Z-scheme phoatocatalytic system was also fabricated when taking $Nb_{3.49}N_{4.56}O_{0.44}$ as an electron collector for TaON. It is expected that $Nb_{3.49}N_{4.56}O_{0.44}$ can also be used to construct other oxynitride-based solid state Z-scheme systems. These results indicate the potential for designing and preparing highly efficient photocatalytic systems by mimicking the nature photosynthesis for photocatalytic water splitting and other environmental issues.

Appendix A. Supplementary data

Supplementary data associated with this article can be found, in the online version, at http://dx.doi.org/10.1016/j.apcatb.2015.10.040.

References

[1] T. Hisatomi, J. Kubota, K. Domen, Chem. Soc. Rev. 43 (2014) 7520–7535.
[2] K. Maeda, ACS Catal. 3 (2013) 1486–1503.
[3] K. Maeda, M. Higashi, D. Lu, R. Abe, K. Domen, J. Am. Chem. Soc. 132 (2010) 5858–5868.
[4] A. Kudo, MRS Bull. 36 (2011) 32–38.
[5] M. Kobayashi, S. Masaoka, K. Sakai, Angew. Chem. 51 (2012) 7431–7434.
[6] K. Maeda, D. Lu, K. Domen, ACS Catal. 3 (2013) 1026–1033.

[7] D.J. Martin, P.J. Reardon, S.J. Moniz, J. Tang, J. Am. Chem. Soc. 136 (2014) 12568–12571.
[8] Y.-C. Pu, W.-H. Lin, Y.-J. Hsu, Appl. Catal. B: Environ. 163 (2015) 343–351.
[9] Y. Chai, J. Ding, L. Wang, Q. Liu, J. Ren, W.-L. Dai, Appl. Catal. B: Environ. 179 (2015) 29–36.
[10] H. Li, Y. Sun, B. Cai, S. Gan, D. Han, L. Niu, T. Wu, Appl. Catal. B: Environ. 170–171 (2015) 206–214.
[11] Y. Bu, Z. Chen, C. Sun, Appl. Catal. B: Environ. 179 (2015) 363–371.
[12] S.S. Ma, K. Maeda, T. Hisatomi, M. Tabata, A. Kudo, K. Domen, Chem. Eur. J. 19 (2013) 7480–7486.
[13] H. Tada, T. Mitsui, T. Kiyonaga, T. Akita, K. Tanaka, Nat. Mater. 5 (2006) 782–786.
[14] L. Liao, Q. Zhang, Z. Su, Z. Zhao, Y. Wang, Y. Li, X. Lu, D. Wei, G. Feng, Q. Yu, X. Cai, J. Zhao, Z. Ren, H. Fang, F. Robles-Hernandez, S. Baldelli, J. Bao, Nat. Nanotechnol. 9 (2014) 69–73.
[15] P. Zhou, J. Yu, M. Jaroniec, Adv. Mater. 26 (2014) 4920–4935.
[16] H. Li, Y. Zhou, W. Tu, J. Ye, Z. Zou, Adv. Funct. Mater. (2015), n/a-n/a.
[17] Y. He, L. Zhang, B. Teng, M. Fan, Environ. Sci. Technol. 49 (2015) 649–656.
[18] Z. Zhang, J.T. Yates Jr., Chem. Rev. 112 (2012) 5520–5551.
[19] K. Maeda, Phys. Chem. Chem. Phys. 15 (2013) 10537–10548.
[20] A. Tyutyunnik, J. Grins, G. Svensson, J. Alloys Compd. 278 (1998) 83–91.
[21] R. Marschall, Adv. Funct. Mater. 24 (2014) 2421–2440.
[22] K. Maeda, K. Teramura, D. Lu, T. Takata, N. Saito, Y. Inoue, K. Domen, Nature 440 (2006) 295.
[23] K. Maeda, K. Teramura, K. Domen, J. Catal. 254 (2008) 198–204.
[24] T. Ohno, L. Bai, T. Hisatomi, K. Maeda, K. Domen, J. Am. Chem. Soc. 134 (2012) 8254–8259.
[25] T.I. Quickenden, T.A. Green, D. Lennon, J. Phys. Chem. 100 (1996) 16801–16807.
[26] Q. Wang, T. Hisatomi, S.S.K. Ma, Y. Li, K. Domen, Chem. Mater. 26 (2014) 4144–4150.
[27] W.-Y. Lin, J. Electrochem. Soc. 140 (1993) 2477.
[28] H. Kyung, J. Lee, W. Choi, Environ. Sci. Technol. 39 (2005) 2376–2382.
[29] R.C. Weast, CRC Handbook of Chemistry and Physics, 60th ed., CRC Press, Boca Raton, Fl, USA, 2015, pp. 980.
[30] W. Yang, L. Zhang, Y. Hu, Y. Zhong, H.B. Wu, X.W. Lou, Angew. Chem. Int. Ed. 51 (2012) 11501–11504.
[31] Y.-P. Yuan, L.-W. Ruan, J. Barber, S.C. Joachim Loo, C. Xue, Energy Environ. Sci. 7 (2014) 3934–3951.
[32] K. Maeda, T. Takata, M. Hara, N. Saito, Y. Inoue, H. Kobayashi, K. Domen, J. Am. Chem. Soc. 127 (2005) 8286–8287.
[33] N. Zhang, M.Q. Yang, S. Liu, Y. Sun, Y.J. Xu, Chem. Rev. 115 (2015) 10307–10377.
[34] Y. Zhou, G. Chen, Y. Yu, Z. Han, J. Pei, J. Sun, F. He, RSC Adv. 4 (2014) 29555.
[35] J. Yuan, Q. Wu, P. Zhang, J. Yao, T. He, Y. Cao, Environ. Sci. Technol. 46 (2012) 2330–2336.
[36] Y. Yu, Y. Tang, J. Yuan, Q. Wu, W. Zheng, Y. Cao, J. Phys. Chem. C 118 (2014) 13545–13551.
[37] T. Hirai, K. Maeda, M. Yoshida, J. Kubota, S. Ikeda, M. Matsumura, K. Domen, J. Phys. Chem. C 111 (2007) 18853–18855.
[38] M. Yoshida, T. Hirai, K. Maeda, N. Saito, J. Kubota, H. Kobayashi, Y. Inoue, K. Domen, J. Phys. Chem. C 114 (2010) 15510–15515.
[39] Y. Zhou, G. Chen, Y. Yu, Y. Feng, Y. Zheng, F. He, Z. Han, Phys. Chem. Chem. Phys. 17 (2015) 1870–1876.
[40] L. Kronik, Surf. Sci. Rep. 37 (1999) 1–206.
[41] T.K. Townsend, N.D. Browning, F.E. Osterloh, Energy Environ. Sci. 5 (2012) 9543.
[42] L.J. Zhang, S. Li, B.K. Liu, D.J. Wang, T.F. Xie, ACS Catal. 4 (2014) 3724–3729.
[43] S.R. Morrison, Electrochemistry at Semiconductor and Oxidized Metal Electrodes, Plenum Press, New York, 1980, pp. 153–188.
[44] J.A. Seabold, K.-S. Choi, Chem. Mater. 23 (2011) 1105–1112.
[45] G. Liu, J. Shi, F. Zhang, Z. Chen, J. Han, C. Ding, S. Chen, Z. Wang, H. Han, C. Li, Angew. Chem. Int. Ed. 53 (2014) 7295–7299.
[46] Y. Wang, Y. Wang, R. Jiang, R. Xu, Ind. Eng. Chem. Res. 51 (2012) 9945–9951.
[47] Z. Yi, J. Ye, N. Kikugawa, T. Kako, S. Ouyang, H. Stuart-Williams, H. Yang, J. Cao, W. Luo, Z. Li, Y. Liu, R.L. Withers, Nat. Mater. 9 (2010) 559–564.
[48] A. Ishikawa, T. Takata, J.N. Kondo, M. Hara, H. Kobayashi, K. Domen, J. Am. Chem. Soc. 124 (2002) 13547–13553.
[49] R. Abe, M. Higashi, K. Domen, J. Am. Chem. Soc. 132 (2010) 11828–11829.
[50] M.Y. Tsang, N.E. Pridmore, L.J. Gillie, Y.H. Chou, R. Brydson, R.E. Douthwaite, Adv. Mater. 24 (2012) 3406–3409.
[51] M. Higashi, K. Domen, R. Abe, J. Am. Chem. Soc. 134 (2012) 6968–6971.
[52] D. Wang, T. Hisatomi, T. Takata, C. Pan, M. Katayama, J. Kubota, K. Domen, Angew. Chem. Int. Ed. 52 (2013) 11252–11256.
[53] J. Hou, C. Yang, H. Cheng, S. Jiao, O. Takeda, H. Zhu, Energy Environ. Sci. 7 (2014) 3758–3768.